Three-dimensional nanotube electrode arrays for hierarchical tubular structured high-performance pseudocapacitors

8 authors, including:

Yuan Gao
The Hong Kong University of Science and T…
7 PUBLICATIONS **207** CITATIONS

SEE PROFILE

Qingfeng Lin
University of Southern California
30 PUBLICATIONS **494** CITATIONS

SEE PROFILE

Wen Li Wang
Soochow University (PRC)
3 PUBLICATIONS **0** CITATIONS

SEE PROFILE

Zhiyong Fan
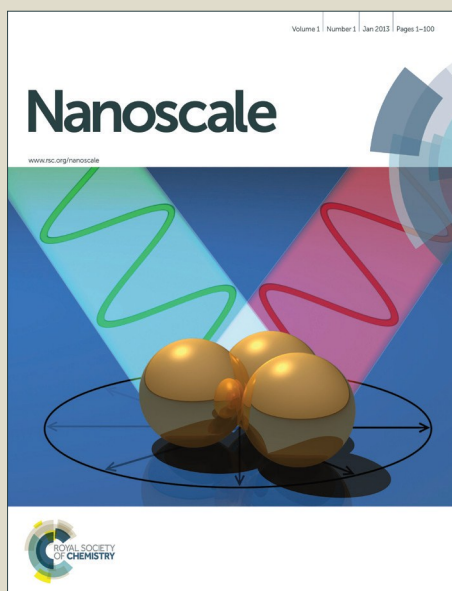The Hong Kong University of Science and T…
133 PUBLICATIONS **6,714** CITATIONS

SEE PROFILE

Nanoscale

PAPER

Three-dimensional nanotube electrode arrays for hierarchical tubular structured high-performance pseudocapacitors

Yuan Gao,[a] Yuanjing Lin,[a] Jiaqi Chen,[a] Qingfeng Lin,[a] Yue Wu,[a] Wenjun Su,[b] Wenli Wang,*[c,d] Zhiyong Fan*[a]

Ordered three-dimensional (3-D) tubular arrays are highly attractive candidates for high performance pseudocapacitors electrodes. Here, we report 3-D fluorine doped tin oxide (FTO) tubular arrays fabricated by a cost-effective ultrasonic spray pyrolysis (USP) method in anodic alumina oxide (AAO) channels with high uniformity. The large surface area of such structure leads to remarkable surface area enhancement up to 51.8 times as compared to a planar structure. Combing with electrochemically deposited manganese dioxide (MnO_2) nanoflakes on the inner side wall of the FTO nanotubes, the unique hierarchical tubular structured pseudocapacitor electrode demonstrated the highest areal capacitance of 193.8 mF cm^{-2} at the scan rate of 5 mV s^{-1} and 184 mF cm^{-2} at the discharge current density of 0.6 mA cm^{-2}, which is 18.5 times of that of a planar electrode. And it also showed a volumetric capacitance of 112.6 F cm^{-3} at the scan rate of 5 mV s^{-1} and 108.8 F cm^{-3} at the discharge current density of 0.6 mA cm^{-2}. In addition, cyclic stability test also indicated that a nanostructured pseudocapacitive electrode has a much larger capacitance retention after 3,000 cycles charge-discharge process as compared with a planar electrode, primarily due to the mechanical stability of the nanostructure. Moreover, pseudocapacitor device fabricated based on such electrodes shows the volumetric capacitance of 17.5 F cm^{-3}, and the highest specific energy of 1.56×10^{-3} Wh cm^{-3}. With the merit of facile fabrication procedures and largely enhanced electrochemical performance, such a 3-D structure has high potency for energy storage systems for a wide range of practical applications.

Introduction

Driven by the surge of energy consumption in a broad range of applications, such as portable electronics, communication, and transportation, high performance energy storage systems are in urgent need worldwide. As attractive alternatives or complement for electrochemical batteries, supercapacitors have appealing attributes including much faster charge – discharge rate, higher power density, longer cycle life time, and thus could serve as promising energy back-up in electric vehicles, unmanned aircrafts, as well as micro self-powered systems, *etc*.[1-4] Pseudocapacitor is one type of widely studied supercapcitor with high performance utilizing surface chemical redox reaction to store electrical charge.[5-8] In such a device, electrode surface area is one of the key factors determining the performance of the device, besides the intrinsic properties of electrode materials. In this regard, fabrication of nanostructured electrodes have been widely explored, mainly due to the fact that they have large electrode surface area thus can significantly improve device overall capacitance.[9-18] Among different nanostructures, ordered

three-dimensional (3-D) tubular arrays are regarded as the one of the most promising structures as electrochemical electrodes,[19-32] mainly due to the facts that i) this structure has large internal surface area for more pseudo-capacitive material deposition;[18, 33] ii) an ordered tubular structure with uniform pore size can help to improve accessibility of electrolyte to electrodes and thus favors fast ion diffusion and electron transport;[33, 34] iii) pseudocapactive material deposited on 3-D nanostructures can withstand more volumetric expansion during the electrochemical reaction as 3-D structures can help to release mechanical stress.[33, 34] These features bring in synergic improvement of electrodes performance based on the combination of effective nanostructures and pseudocapactive materials.[18]

There are a number of different approaches to fabricate tubular structures, such as top-down lithographic methods and bottom-up self-organized approaches. Top-down approaches are typically expensive and have limited scalability. Meanwhile, bottom-up approaches in principle are much more cost-effective. Among various types of bottom-up approaches, anodization of valve metals, including Aluminum (Al), Titanium (Ti), *etc*., can lead to formation of the highly packed oxide nanotubular

Nanoscale

View Article Online
DOI: 10.1039/C6NR03337G

Page 2 of 8

Journal Name

ARTICLE

structures via self-organizing mechanisms.[25, 35, 36] And this approach has been proven highly scalable with cost-effectiveness.[37] In this work, anodic alumina oxide (AAO) membranes with highly ordered 3-D nanotube arrays were fabricated with nanoimprint in conjunction with electrochemical anodization. And the membranes were then utilized to fabricate high performance pseudocapacitors. Such an architecture has fairly large surface area which can benefit the performance of the devices. It is known that an AAO is not conductive by itself, therefore a low-cost ultrasonic spray pyrolysis (USP) process was utilized to deposit conductive fluorine doped tin oxide (FTO) tubular structured electrodes inside AAO pores. In this case, the FTO tubes have highly uniform side wall thickness which can be precisely controlled by spraying conditions. The tubular FTO electrodes are mechanically robust due to the support of AAO scaffold. And a 20 μm thick structure has 51.8 times surface area of that of a planar electrode with the same projection area. In this work manganese dioxide (MnO_2) was chosen as the pseudocapacitive material deposited on FTO electrodes to demonstrate the device concept due to the fact that it has the advantages of high theoretical specific capacitance (~1370 F g^{-1}), low cost (less than one dollar per pound for the metal) and it is environmentally friendly, etc.. This material has been widely used as a pseudocapacitive material for many supercapacitor devices.[2] In addition, nanoflakes MnO_2 were electrochemically deposited on the internal surface of FTO tubular electrodes forming unique hierarchical tubular pseudocapacitor device structure which further enlarges the electrode surface area for more ion diffusion and redox reaction. And thus, the electrode has high volumetric capacitance of 112.6 F cm^{-3} (10 μm thick AAO) and areal capacitance of 193.8 mF cm^{-2} (20 μm electrode) respectively. This areal capacitance is 18.5 times of that of a planar FTO substrate. These results have shown that such low cost spray process is highly promising for practical fabrication of effective nanostructures to obtain high performance pseudocapacitors.
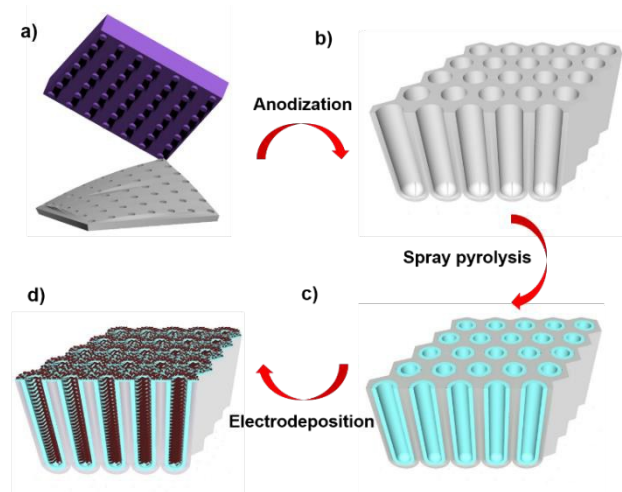
Results and discussion

Fig. 1. Schematic illustration showing the fabrication process of hierarchical tubular pseudocapacitor electrodes. a) Nanoimprint process with hexaganol nanopillars Si mold. b) As-prepared AAO membranes after anodization and Al removal. c) USP deposition of FTO tubular arrays. d) Hierarchical tubular electrode achieved by MnO_2 electrodeposition.

The fabrication process of the hierarchical nanotube pseudocapacitive electrodes mainly comprises 4 steps as shown in Fig. 1: i) nanoimprint on an Al foil to leave ordered indentation (Fig. 1a); ii) electrochemical anodization to form an AAO membrane with perfect hexagonal ordering (Fig. 1b); iii) conformal and uniform deposition of FTO tubular structures into AAO nanochannels with USP method (Fig. 1c); iv) homogenenous electrodeposition of MnO_2 nanoflakes into FTO tubular arrays to achieve hierarchical electrodes (Fig. 1d). Optical images of electrodes after different fabrication steps could be found in Fig. S1a. It is worth mentioning that to form conductive nanotubular structures, atomic layer deposition (ALD) and physical vapor deposition (PVD) methods have been mostly adopted in the past.[19, 21, 22, 28] However, PVD method is not suitable for long channel high aspect ratio structure deposition due to directionality of the vapor molecules. And the rather high cost and slow deposition rate of ALD also limits its application for practical devices. By contrast, in such fabrication scheme, USP process is simply conducted in atmospheric pressure in a fumehood (Fig. S1b), and the process is not only of low-cost, but also suitable for conformal deposition of materials in high aspect ratio structure.
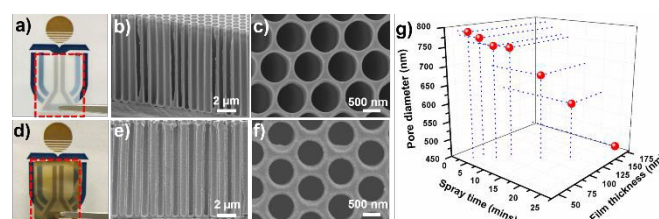

Fig. 2. Optical and SEM images of freestanding AAO tubular arrays with the length of 10 μm before USP, a-c). Optical and SEM images of freestanding AAO tubular arrays with the length of 10 μm after USP, d-f). g) Pore diameter and Film thickness as the functions of USP time.

Fig. 2a-f show the Optical image and scanning electron microscopy (SEM) images of 10 μm depth freestanding AAO tubular arrays before and after FTO deposition. Obviously, the color of AAO backbone has been changed from transparent to homogeneous brown, proving the deposition of FTO inside AAO channels and the dense FTO film is conformally and uniformly deposited on the AAO scaffolds, which can be seen in Fig. e and f. Fig. 2g shows the FTO tube inner diameter and film thickness as the functions of spray time, with the AAO initial pore diameter of 900 nm (Fig. 2c). The FTO tube inner diameter decreases at the average rate of 11 nm min^{-1} during USP deposition process, simultaneously with the increasing thickness of FTO film at the average deposition rate of 5.2 nm min^{-1} (Fig. S2a). Such a good linear relationship with the spray time demonstrates the precise controllability of USP deposition method. To further confirm this, the same process was repeated on the 20 μm depth AAO tubular arrays. In these samples, the thickness of FTO film increases at the average deposition rate of 7.8 nm min^{-1}, while the FTO inner diameter decreases at the average rate of 15.8 nm min^{-1} (Fig. S2b and c). For applications such as pseudocapacitor electrodes, a naturally large surface area is preferred to accommodate more active material. To attain a large surface area, the pore size was enlarged to 900 nm by wet etch which is already 90% of the periodicity, and a layer of FTO with the thickness of around 100 nm was deposited into both 10 μm and 20 μm AAO tubular arrays. Without removing AAO scaffold, the highly ordered structural integrity is well maintained addressing nanostructure collapse issue in some other reports.

And the corresponding surface area enhancement are nearly 26.4 (10 μm) and 51.8 times (20 μm) of that of the planar structure. The detailed calculation method could be seen from Fig. S3a and b.
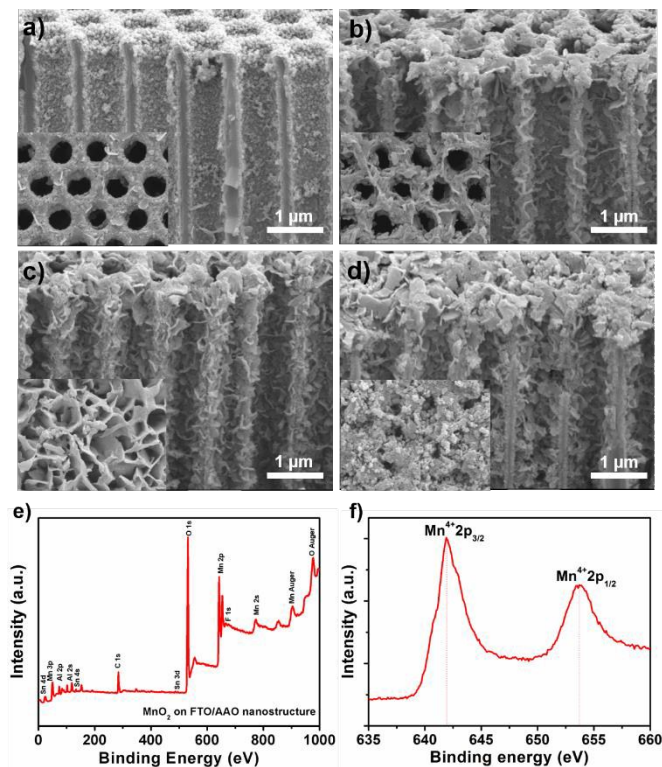

Fig. 3. SEM images of hierarchical tubular electrodes (10 μm length) at different electrodeposition time a) 45 s. b) 60 s. c) 75 s. d) 90 s. e) XPS spectrum of hierarchichal tubular electrode and f) Mn 2p level characterization.

In order to realize hierarchical tubular structured pseudocapacitor electrodes, MnO_2 was deposited into the FTO tubular arrays with pulse electrochemical deposition. To obtain the optimized performance, a systematically study was conducted on 10 μm depth FTO tubular arrays via controlling the deposition time. Fig. 3a-d show the cross-sectional view and top view SEM images of the structures after different deposition time of 45 s, 60 s, 75 s and 90 s, respectively. Interestingly, it was found that MnO_2 nanoflakes rather than a thin film were uniformly deposited onto inner side wall of FTO tubular arrays. The interleaved morphology of MnO_2 nanoflakes together with FTO form the hierarchical tubular pseudocapacitor electrodes, and such electrodes could further enhance the surface area for more ion contact and facilitate ion transport vertically along the channels together horizontal transport along the nanoflakes surface. Nevertheless, it can also be seen that the channel diameter becomes smaller and smaller as the amount of MnO_2 increases and it is nearly closed after 90 s electrodeposition (inserted in Fig. 3d), leaving the surface a non-ordered structure (Fig. 3d). Such random structure generates large ion transport resistance, which prevents ion from diffusing into deep channels, and thus leading to poor rate capability. X-ray photoelectron spectroscopy (XPS) of as-built hierarchical tubular electrode is shown in Fig. 3e. Six elements (Sn, Mn, Al, C, O, F) are identified at the surface of the electrode. The appearance of Sn, Al and F is attributted to AAO backbone and FTO conductive

layer. Mn stems from MnO_2 achieved by electrodeposition. The trace of O mainly comes from metal oxide, and C together with the rest of O is from adventitious contamination. According to Fig. 3e, two peaks at 641.9 eV and 653.7 eV can be identified, which indicates the Mn^{4+} ions are dominant in the deposited material. The detailed chemical composition of hierarchical tubular electrodes was probed by energy dispersive spectrometer (EDS), shown in Fig. S4. Different methods for materials characterization are shown in Fig. S9. According to Raman spectrum shown in Fig. S9a sharp peak located at 650 cm^{-1} proves the existence of MnO_2, which is attributed to the stretching vibration of MnO_6 octahedral molecules. Fourier transform infrared spectroscopy (FTIR) result is shown in Fig. S9b. The lack of strong absorption peak at the wavenumber of 3500 cm^{-1} proves that most of the pseudocapacitive materials comes from metal oxide instead of metal hydroxide. X-ray diffraction (XRD) measurement was based on materials components of entire pseudocapacitor electrode to investigate the crystallographic structure of the materials, which can be seen in Fig. S9c.
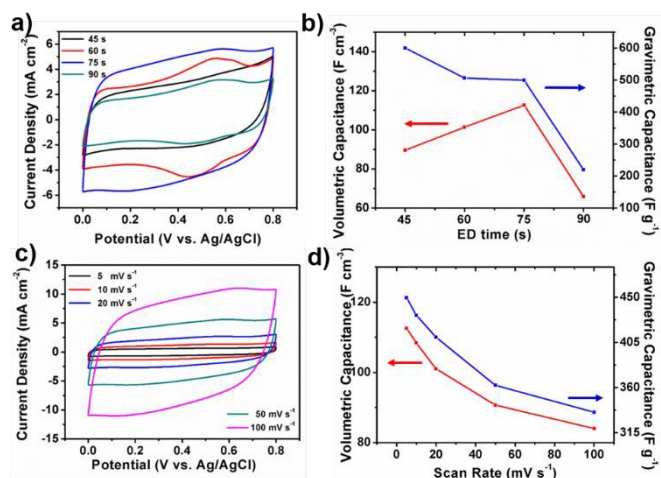

Fig. 4. a) CV curve of 10 μm hierarchical tubular electrodes after different electrodeposition time at the scan rate of 50 mV s^{-1}. b) Volumetric Capacitance and Gravimetric Capacitance of 10 μm hierarchical tubular electrodes as the functions of electrodeposition time at the scan rate of 5 mV s^{-1}. c) CV curves of different scan rate after 75 s electrodeposition. d) Volumetric Capacitance and Gravimetric Capacitance of 75 s electrodeposition as the functions of scan rate.

To evaluate the electrochemical performance of hierarchical tubular electrodes, cyclic voltammetry (CV) measurements with a three-electrode configuration on the as-prepared electrode with 0.6 cm × 0.5 cm footprint area was conducted in 1 M Na_2SO_4 liquid electrolyte with voltage ranging from 0 to 0.8 V. In such configuration, MnO_2 decorated FTO tubular arrays was defined as working electrode, saturated Ag/AgCl served as a reference electrode and carbon rod served as a counter electrode. The distance of the neighbouring electrode was 3 cm. Fig. 4a presents the typical CV curves at the scan rate of 50 mV s^{-1} after different electrodeposition time. The much more rectangular shape and larger area enclosed by CV curves demonstrate that the optimized capacitance could be achieved after 75 s electrodeposition. Note that volumetric capacitance and gravimetric capacitance are both important of Figure-of-merits of a pseudocapacitor, they can be calculated by using the following equations:

Nanoscale

View Article Online
DOI: 10.1039/C6NR03337G

Page 4 of 8

ARTICLE

Journal Name

$$C_v = \int_0^{0.8} \left(\left| I_{FTO/MnO_2} \right| - \left| I_{FTO} \right| \right) dU / 2V_0 \Delta U v_0 \qquad 1)$$

$$C_v = it / \Delta U V_0 \qquad 2)$$

$$C_g = \int_0^{0.8} \left(\left| I_{FTO/MnO_2} \right| - \left| I_{FTO} \right| \right) dU / 2m \Delta U v_0 \qquad 3)$$

$$C_g = it / \Delta U m \qquad 4)$$

$$m = QM / 2e N_A \qquad 5)$$

where C_v and C_g are volumetric capacitance and gravimetric capacitance of the hierarchical tubular pseudocapacitive electrode, respectively. m and V_0 are the mass of MnO_2 and the volume of the entire electrode including AAO scaffold. I is the electrical current driven by voltage, i is the discharge current, U is the voltage, ΔU is the operating voltage window (0.8 V), v_0 is the scan rate. Q is the amount of charge passing through the entire electrode, M is the molecular weight of MnO_2, e is the electronic charge, and N_A is the Avogadro's number. Note that the mass loading of MnO_2 after 45 s, 60 s, 75s, 90 s, electrodeposition are 0.151 mg cm^{-2}, 0.201 mg cm^{-2}, 0.251 mg cm^{-2}, 0.301 mg cm^{-2}, respectively, normalized to the projected area of electrode. Fig. 4b shows the volumetric capacitance and gravimetric capacitance of hierarchical tubular electrodes at the scan rate of 5 mV s^{-1} as functions of electrodeposition time. The peak value of volumetric capacitance can be achieved from the device with 75 s MnO_2 electrochemical deposition, while longer and shorter deposition time both show lower volumetric capacitance. This is due to the fact that volumetric capacitance is normalized to the volume of the entire electrode, augement of MnO_2 mass loading by prolonging deposition time increases overall capacitance. However, excessively long deposition time leads to closing of ion transportation channels, as shown in Fig. 3d, this causes loss of overall capacitance. As for gravimetric capacitacne, it monotonically decreases when increasing deposition time as shown in Fig. 4b. This is because gravimetric capacitance is normalized to the net MnO_2 mass loading, normally more mass loading increases material thickness that slows down charge transport inside MnO_2 material since it has poor charge mobility. In theory, a thinner layer of MnO_2 can lead to higher gravimetric capacitance, as reported in a number of prior literature.[8, 20, 33] However from a practical standpoint, it is more meaningful to normalize the capacitance with total electrode or device volume and/or weight,[1, 38] and such performance were plotted in Fig. S5a and b. Obviously, both the highest new gravimetric capacitance and volumetric capacitance were achieved after 75 s deposition, proving the optimized material thickness. Fig. 4c shows the CV curves of an electrode with 75 s MnO_2 deposition at different scan rates. The quasi-rectangular shape with a nearly mirror image of current at the increasing scan rate further confirms that 75 s deposition of MnO_2 on such a three-dimensional structure leads to an excellent pseudocapacitive performance. Basically, no obvious redox peak could be observed for MnO_2 pseudocapacitors because of the continuous redox reaction between Mn(III) and Mn(IV),[2] and we attributed the obvious redox peak occured in this work to the incomplete redox reaction between MnO_2 and metal ions. CV curves of electrodes with 30 s, 45 s, and 90 s MnO_2 deposition time at different scan rates are plotted in Fig. S7a-c. The volumetric capacitance and gravimetric capacitance for 75 s deposition as the fucntions of scan rate are plotted in Fig. 4d. The highest specific capacitances are 112.6 F cm^{-3} and 449.5 F g^{-1} at the scan rate of 5 mV s^{-1} and the corresponding values are 108.8

F cm^{-3} and 434.3 F g^{-1} at the discharge current density of 0.6 mA cm^{-2}. To further study the composition of total capacitance, CV and Galvanostatic charge-discharge (GCD) characterization were also performed based on 10 μm bare FTO and pseudocapacitor electrode with 75 s deposition, which are shown in Fig. S6. The negligible electrical double layer capacitance, around 1.5 mF cm^{-2} at the discharge current density of 0.6 mA cm^{-2} comes from bare FTO demonstrates little effect on the total capacitance. The areal capacitance, gravimetric capacitance, volumetric capacitance of different deposition time at different scan rates are also shown in Fig. S7d-f.
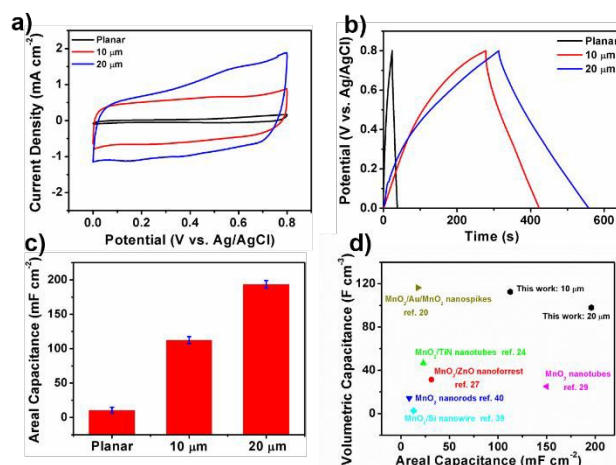

Fig. 5. a) CV comparison among planar electrode, 10 μm hierarchical tubular electrode and 20 μm hierarchical tubular electrode at the scan rate of 5 mV s^{-1}. b) GCD comparison among planar electrode, 10 μm hierarchical tubular electrode, 20 μm hierarchical tubular electrode at the current density of 0.6 mA cm^{-2}. c) Areal Capacitance comparison among planar electrode, 10 μm hierarchical tubular electrode, 20 μm hierarchical tubular electrode at the scan rate of 5 mV s^{-1} with the error bars. d) Volumetric Capacitance as the function of areal capacitance for different nanostructured electrode.

To further explore the practical merit of such hierarchical tubular electrodes, 75 s MnO_2 electrodeposition at the same current density was conducted on a 3-D FTO tube arrays with 20 um depth, and the SEM images are shown in Fig. S8a and b. In order to further show the advantage of hierarchical tubular electrodes, MnO_2 was also deposited onto a planar glass substrate deposited with an FTO film, serving as a control sample for comparison. For the sake of a fair comparison, the amount of MnO_2 was the same as compared with that on 20 μm hierarchical tubular electrode. Fig. 5a presents the CV curve of different electrodes at the scan rate of 5 mV s^{-1}. The largest area surrounded by the CV curve shows that 20 μm hierarchical tubular electrode has the highest capacitance. By contrast, the irregular shape and smallest area enclosed by CV curve based on planar electrode demonstrate the poor pseudocapacitive behavior. GCD characteristics at the current density of 0.6 mA cm^{-2} based on different architectures are also plotted in Fig. 5b. Notably, the longest discharge time of 20 μm hierarchical tubular electrode demonstrates more charge stored in the electrode with more complete redox reaction for the active material on the surface. Such results could be rationalized by considering the fact that the nanostructured electrodes always achieve thinner MnO_2 deposition on surface as compared to the planar control sample with the same MnO_2 mass loading due to much larger surface area, therefore, both ion diffusion length and electron transport

length are much shortened, leading to the lowered resistance for charge transport. GCD based on 10 μm and 20 μm hierarchical tubular electrodes at different current density are plotted in Fig. S10a and b. Fig. 5c shows the areal capacitance of different electrodes. It is worth mentioning that 20 μm hierarchical tubular electrode achieved areal capacitance of 193.8 mF cm^{-2} at the scan rate of 5mV s^{-1} and 184 mF cm^{-2} at the discharge current density of 0.6 mA cm^{-2}, however, only 10.6 mF cm^{-2} was obtained from the planar electrode, nearly 18.5 times of performance enhancement factor is achieved even they have the same MnO$_2$ mass loading. The little mismatched enhancement between surface area and electrochemical performance could result from the difficulty of the ion diffusion caused by channel narrowing down after electrodeposition. And this enhancement factor is nearly 4.3 times of our previously reported results on nanospike electrodes.[20] Note that we avoid the use of volumetric capacitance for comparison between the hierarchical tubular electrodes and planar electrodes, as the latter is fabricated on thick glass supporting substrate, it is not a fair comparison if the capacitance is normalized to the entire electrode including glass substrate. In terms of volumetric capacitance, 20 μm electrode achieved 96.9 F cm^{-3} at the scan rate of 5 mV s^{-1} and 92 F cm^{-3} at the discharge current density of 0.6 mA cm^{-2} (Fig. S10c and d), which is slightly lower than that of 10 μm electrode (112.6 F cm^{-3}). Such a result could be attributed to the larger series resistance along FTO nanotubes when the channel length of the electrode increases, and also longer ion diffusion time in deeper channels. Typically, obtaining higher areal capacitance can lead to occupying larger electrode volume and thus, there is a trade off between high areal capacitance and volumetric capacitance. In this work, we have successfully achieved respectably high values on both capacitances, and these values are significantly higher than many previous reported results,[20, 24, 27, 29, 39, 40] as shown in Fig. 5d.
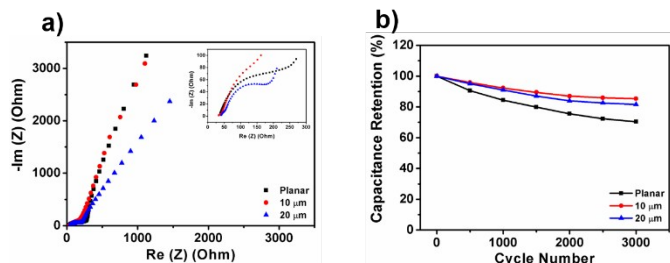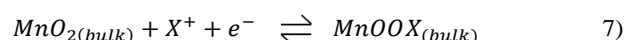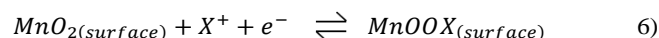

Fig. 6. a) Nyquist plots of planar electrode, 10 μm hierarchical tubular electrode, 20 μm hierarchical tubular electrode. b) Cycling performance of planar electrode, 10 μm hierarchical tubular electrode, 20 μm hierarchical tubular electrode during 3000 cycles at the scan rate of 100 mV s^{-1}.

To further examine the electrochemical performance of the hierarchical structured electrode, electrochemical impedance spectroscopy (EIS) measurements were conducted in the frequency range from 100 kHz to 0.01 Hz and the result is shown in Fig. 6a. It is clear to see that the planar electrode has the largest radius for the semicircle in the high frequency range (inserted in Fig. 6a), which reflects the largest charge-transfer resistance compared with nanostructured hierarchical tubular electrodes. Moreover, the linear region at the low frequency region are controlled by the Warburg impedance, defined as the diffusion resistance of the metal alkali ions. The intersection of X axis and the reversed extension line at the low frequency reflects the value of Warburg coefficient (σ), and such value is direct proportional to the Warburg impedance (R$_w$). In this way, the larger portion

of Warburg impedance region at the low frequency further demonstrates that planar electrode hinders the diffusion of the ions. In addition, the linear region at low frequency could also be regarded as the semi-infinite diffusion model, and the slightly deviated value for the slope from 1 is because the reaction occurs at the electrode surface is not merely controlled by electrode potential but other state variables. Cyclic stability test was also conducted on both nanostructured and planar electrodes at the scan rate of 100 mV s^{-1}, which could be seen in Fig. 6b. Specifically, 85.4 % and 81.6 % capacitance retention were achieved for 10 μm and 20 μm hierarchical tubular electrodes after 3,000 cycles of test. However, it is only 70.3% for planar electrode, and such result could be explained by the charge storage mechanism in pseucocapacitive materials. The charge storage process mainly consists of i) surface redox reaction; ii) intercalation of ions in the bulk materials,[34] which could be described according to the following formular:

$$MnO_{2(surface)} + X^+ + e^- \;\rightleftharpoons\; MnOOX_{(surface)} \qquad 6)$$

$$MnO_{2(bulk)} + X^+ + e^- \;\rightleftharpoons\; MnOOX_{(bulk)} \qquad 7)$$

where X$^+$ refers to cation in the electrolyte, such as Li$^+$, Na$^+$, etc. The volumetric expansion during the test compromised the performance stability of planar electrode, and after hundreds of cycles, MnO$_2$ was exfoliated from the planar substrate, which could be seen from Fig. S11a and b. However, a nanostructure based electrode could withstand more volume expansion due to the anchor effect protection from the 3D backbones, and thus showing more stable capacitance retention (Fig. S11c and d).
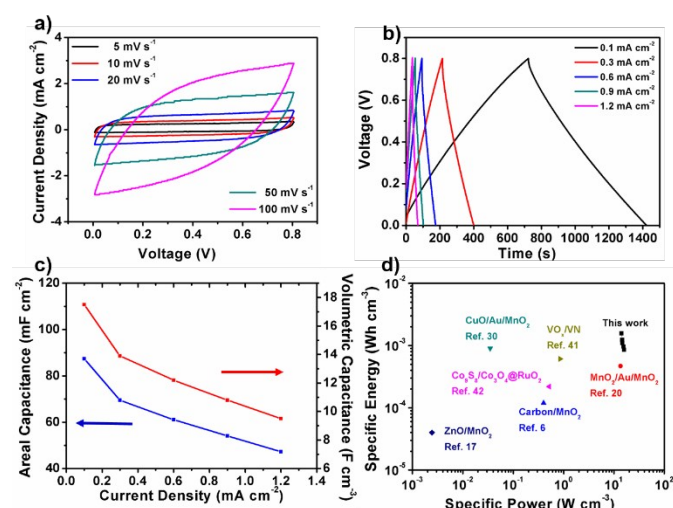

Fig. 7. a) CV curves of symmetric supercapacitor at different scan rates. b) GCD curve of symmetric supercapacitor device with different current densities. c) Areal Capacitance and Volumetric Capacitance of supercapacitor device calculated based on different current densities. d) Ragone plot shows the specific energy and specific power of the device.

The symmetric pseudocapacitor device was further fabricated to elucidate the advantages of such hierarchical structure. CV curve and GCD were plotted in Fig. 7a and b. The highest areal capacitance and volumetric capacitance for the device occur at the discharge current density of 0.1 mA cm^{-2} and the corresponding performance are 87.4 mF cm^{-2} and 17.5 F cm^{-3}, respectively. Note that the volume of the total device includes two pseudocapacitor electrodes with the same thickness of 20

Nanoscale

View Article Online

DOI: 10.1039/C6NR03337G

Page 6 of 8

Journal Name

ARTICLE

μm and seperator with the thickness of 10 μm and the solid state electrolyte. For the practical application, specific energy and specific power are the two pivotal benchmarks for pseudocapacitors, which could be calculated from the following equations:

$$E = C_v(\Delta E)^2/2 \qquad 8)$$

$$P = (\Delta E)^2/4RV \qquad 9)$$

$$R = U_{drop}/2i \qquad 10)$$

Where E and P are the specific energy and specific power of the device. ΔE is the voltage window of the device exluding the voltage drop (U_{drop}), V is the volume of total device, R is the internal resistance of the device. Ragone plot was shown in Fig. 7d and the highest specific energy is 1.56×10^{-3} Wh cm^{-3} with the corresponding specific power value of 14.2 W cm^{-3}, and such performance are superior to many previous reports.[6, 17, 20, 30, 41, 42] Moreover, the cyclic stability of the pseudocapacitor device was also tested at the scan rate of 100 mVs^{-1}, which is shown in Fig. S12. It is worth mentioning that the capacitance still maintains 80 % of its initial value after 5,000 cycles, and thus demonstrating the reliable psuedocapacitive behavior of such hierarchical structures.

Conclusions

Herein, we report a three-dimensional hierarchical structure consists of nanotubular FTO and MnO$_2$ nanoflakes deposited inside the FTO nanotubes for high performance pseudocapacitors. The entire electrode structure was fabricated on anodic alumina oxide template with large pore diameter. The FTO nanotube electrodes were fabricated with cost-effective USP process without removing AAO scaffold thus the structural integrity was well maintained. It was discovered that a nanotubular electrode has 51.8 times of surface area as compared to a planar electrode. Thus the hierarchical structured electrodes demonstrated a volumetric capacitance of 112.6 F cm^{-3} normalized to the entire electrode volume, and an areal capacitance of 193.8 mF cm^{-2} normalized to electrode projection area. The unique hierarchical structure leads to a remarkable enhancement in pseudocapacitive capacitance of 18.5 times over a planar electrode with the same MnO$_2$ mass loading. The marginal change of the capacitance after cyclic test further shows that such electrode is highly robust. In addition, pseudocapacitor device fabricated based on such electrode achieves the high volumetric capacitance of 17.5 F cm^{-3}, together with the highest specific energy of 1.56×10^{-3} Wh cm^{-3}. With the merits of low cost fabrication procedures and enhanced electrochemical performance, such three-dimensional hierarchical tubular electrodes are attractive for high performance electrical energy storage devices.

Experimental section

Preparation of AAO tubes. Aluminum foil with the thickness of 0.25 mm and area of 3 cm $\times$ 2 cm was prepared by cutting, followed by electrochemically cleaning under 12 V constant voltage for 2 min. After that, 5 mm $\times$ 5 mm silicon stamps with ordered hexagonal nanopillars with the height of 0.1 μm and pitch of 1 μm were utilized as imprinting mold to produce a nanoindentation array on the surface of as-prepared aluminum foil. Afterwards, the aluminum foil undergoes one-step anodization for AAO tubes for 10 μm and 20 μm under 400 V

direct voltage. Then, AAO tubes with the channel length of 10 μm, 20 μm are immersed into the 5 v % H$_3$PO$_4$ for 65 mins, 70 mins, respectively at the temperature of 53 ℃ to enlarge the pore size. Finally, Al substrate was removed in saturated mercuric chloride to ahieve freestanding AAO tubes.

Preparation of FTO precursor solution. FTO precursor solution was firstly prepared by refluxing. Typically, 21 g SnCl$_4$ 5H$_2$O was added into 300 ml absolute ethanol in a three-necked flask and refluxing for 1 hour with the temperature of 60 ℃, with magnetic stirring to form uniform, stable and transparent solution. Afterwards, 450 mg of NH$_4$F was then dissolved into 10 ml DI water and added drop by drop into the SnCl$_4$/ethanol solution. The refluxing system was maintained for another 3 hours, followed by natural cooling to the room temperature.

Fabrication of FTO tubular arrays. A homemade two-terminal USP equipment was used for FTO deposition, as shown in Fig. S1b. Firstly, AAO samples with the channel length of 10 μm, 20 μm were fixed on the hot plate, and compressed air worked as the carry gas was injected into input terminal of the USP setup. The output terminal was connected with the nozzle which covers AAO substrates. Then the sonicator was turned on to actuate and vaporize the precursor solution. And the compressed air carried precursor vapor to deposit the hot surface of the AAOs. The deposition process is conducted under the temperature of 400 ℃ and lasts for different time. After finishing FTO deposition, the samples are annealed in the Ar atmosphere for 2 hours with the temperature of 500 ℃, followed by naturally cooling to the room temperature.

Fabrication of hierarchical tubular electrodes. FTO tubular arrays with the channel length of 10 μm is used for systematical study of the electrochemical performance of the hierarchical tubular electrode. A galvanostatic square waveform with duty cycle of 1 % and frequency of 1 Hz was applied for pulsed electrochemical deposition. Different amount of MnO$_2$ was electrochemically deposited by precise control the cycles from 4,500 to 9,000 with the constant current of 6.67 mA for the projected 1 cm^2 at room temperature. Later, the same electrodeposition process is conducted based on planar structure and 20 μm FTO tubular arrays and the amount of MnO$_2$ was doubled as compared with 10 μm hierarchical tubular arrays. The deposition solution consists of 0.05 M manganese acetate (MnAc$_2$), 98 % purity and 0.1 M sodium sulfate (Na$_2$SO$_4$), 99 % purity.

Characterization of Samples.

Various analytical techniques were utilized to characterize the as-fabricated nanostructured electrode. Morphologies were characterized using field-emission scanning electron microscopy (JSM-7100F, Japan). Chemical compositions were studied by X-ray photoelectron spectroscopy (PHI 5600, USA) and energy dispersive spectrometer (JSM-7100F, Japan). CV, GCD and EIS measurements based on three-electrode configuration were performed on an electrochemical workstation (Gamry, USA). CV was carried out at different scan rates of 5, 10, 20, 50, 100mV s^{-1}. GCD was measured at 0.6, 1.2, 1.8, 2.4, 3.6 mA cm^{-2}. EIS was measured with the frequency range from 100 kHz to 0.01 Hz with potential amplitude of 10 mV.

Nanoscale Accepted Manuscript

Page 7 of 8

Nanoscale

View Article Online
DOI: 10.1039/C6NR03337G

Journal Name

ARTICLE

Notes and references

[a] Department of Electronic and Computer Engineering, The Hong Kong University of Science and Technology, Clear Water Bay, Kowloon, Hong Kong, China SAR
[b] School of Mechanical Engineering, Xi'an Jiaotong University, Xi'an Shaanxi 710049, China
[c] College of Textile and Clothing Engineering, Soochow University, Suzhou, 215021, China
[d] National Engineering Laboratory for Modern Silk, Suzhou, 215123, China

*Corresponding Author: Zhiyong Fan; E-mail: eezfan@ust.hk
Wenli Wang; E-mail: wlwang@suda.edu.cn

† Electronic Supplementary Information (ESI) available: Optical images of imprint Si mold and USP setup, SEM images of FTO tubular arrays after different spray time, Surface area calculation and Surface area enhancement, EDX of FTO tubular arrays before and after electrodeposition, Raman, FTIR, XRD spectrum for materials characterization, CV, GCD, Gravimetric capacitance, volumetric capacitance and areal capacitance calculation, Optical images of electrode after cyclic test. See DOI: 10.1039/b000000x/

1 J. R. Miller and P. Simon, *Science Magazine,* 2008, **321**, 651-652.

2 P. Simon and Y. Gogotsi, *Nature materials,* 2008, **7**, 845-854.

3 X. Wang, X. Lu, B. Liu, D. Chen, Y. Tong and G. Shen, *Adv Mater,* 2014, **26**, 4763-4782.

4 Y. Gogotsi, *Nature,* 2014, **509**, 568-570.

5 X. Xia, Y. Zhang, D. Chao, C. Guan, Y. Zhang, L. Li, X. Ge, I. M. Bacho, J. Tu and H. J. Fan, *Nanoscale,* 2014, **6**, 5008-5048.

6 X. Xiao, T. Li, P. Yang, Y. Gao, H. Jin, W. Ni, W. Zhan, X. Zhang, Y. Cao and J. Zhong, *Acs Nano,* 2012, **6**, 9200-9206.

7 R. Yi, S. Chen, J. Song, M. L. Gordin, A. Manivannan and D. Wang, *Advanced Functional Materials,* 2014, **24**, 7433-7439.

8 Z. Yu, B. Duong, D. Abbitt and J. Thomas, *Adv Mater,* 2013, **25**, 3302-3306 .

9 M. Zhi, C. Xiang, J. Li, M. Li and N. Wu, *Nanoscale,* 2013, **5**, 72-88.

10 M. Huang, F. Li, F. Dong, Y. X. Zhang and L. L. Zhang, *Journal of Materials Chemistry A,* 2015, **3**, 21380-21423.

11 D. N. Futaba, K. Hata, T. Yamada, T. Hiraoka, Y. Hayamizu, Y. Kakudate, O. Tanaike, H. Hatori, M. Yumura and S. Iijima, *Nature materials,* 2006, **5**, 987-994.

12 X. Lu, M. Yu, G. Wang, T. Zhai, S. Xie, Y. Ling, Y. Tong and Y. Li, *Adv Mater,* 2013, **25**, 267-272.

13 D. Pech, M. Brunet, H. Durou, P. Huang, V. Mochalin, Y. Gogotsi, P. Taberna and P. Simon, *Nature nanotechnology,* 2010, **5**, 651-654.

14 A. L. M. Reddy, S. R. Gowda, M. M. Shaijumon and P. M. Ajayan, *Adv Mater,* 2012, **24**, 5045-5064.

15 X. Xia, D. Chao, Z. Fan, C. Guan, X. Cao, H. Zhang and H. J. Fan, *Nano letters,* 2014, **14**, 1651-1658.

16 X. Xia, Y. Zhang, Z. Fan, D. Chao, Q. Xiong, J. Tu, H. Zhang and H. J. Fan, *Advanced Energy Materials,* 2015, **5**.

17 P. Yang, X. Xiao, Y. Li, Y. Ding, P. Qiang, X. Tan, W. Mai, Z. Lin, W. Wu and T. Li, *ACS nano,* 2013, **7**, 2617-2626.

18 Z. Yu, L. Tetard, L. Zhai and J. Thomas, *Energy & Environmental Science,* 2015, **8**, 702-730 .

19 X. Chen, E. Pomerantseva, P. Banerjee, K. Gregorczyk, R. Ghodssi and G. Rubloff, *Chemistry of Materials,* 2012, **24**, 1255-1261.

20 Y. Gao, H. Jin, Q. Lin, X. Li, M. M. Tavakoli, S. Leung, W. M. Tang, L. Zhou, H. L. W. Chan and Z. Fan, *Journal of Materials Chemistry A,* 2015, **3**, 10199-10204.

21 F. Grote and Y. Lei, *Nano Energy,* 2014, **10**, 63-70.

22 F. Grote, L. Wen and Y. Lei, *J. Power Sources,* 2014, **256**, 37-42.

23 U. N. Maiti, J. Lim, K. E. Lee, W. J. Lee and S. O. Kim, *Adv Mater,* 2014, **26**, 615-619.

24 S. A. Sherrill, J. Duay, Z. Gui, P. Banerjee, G. W. Rubloff and S. B. Lee, *Physical Chemistry Chemical Physics,* 2011, **13**, 15221-15226.

25 Y. Song, Y. Li, J. Guo, Z. Gao and Y. Li, *Journal of Materials Chemistry A,* 2015, .

26 Z. Su, C. Yang, B. Xie, Z. Lin, Z. Zhang, J. Liu, B. Li, F. Kang and C. Wong, *Energy & Environmental Science,* 2014, .

27 X. Sun, Q. Li, Y. Lü and Y. Mao, *Chemical Communications,* 2013, **49**, 4456-4458.

28 L. Wen, Y. Mi, C. Wang, Y. Fang, F. Grote, H. Zhao, M. Zhou and Y. Lei, *Small,* 2014, **10**, 3162-3168.

29 H. Xia, J. Feng, H. Wang, M. O. Lai and L. Lu, *J. Power Sources,* 2010, **195**, 4410-4413.

30 Z. Yu and J. Thomas, *Adv Mater,* 2014, **26**, 4279-4285.

31 Z. Yu, C. Li, D. Abbitt and J. Thomas, *Journal of Materials Chemistry A,* 2014, **2**, 10923-10929.

32 X. Zhang, X. Peng, W. Li, L. Li, B. Gao, G. Wu, K. Huo and P. K. Chu, *Small,* 2015, **11**, 1847-1856.

33 S. Chabi, C. Peng, D. Hu and Y. Zhu, *Adv Mater,* 2014, **26**, 2440-2445.

34 H. Zhao, C. Wang, R. Vellacheri, M. Zhou, Y. Xu, Q. Fu, M. Wu, F. Grote and Y. Lei, *Adv Mater,* 2014, **26**, 7654-7659.

35 S. Leung, L. Gu, Q. Zhang, K. Tsui, J. Shieh, C. Shen, T. Hsiao, C. Hsu, L. Lu, D. Li, Q. Lin and Z. Fan, *Sci. Rep.,* 2014, **4**, 4243.

36 Y. Lin, Q. Lin, X. Liu, Y. Gao, J. He, W. Wang and Z. Fan, *Nanoscale research letters,* 2015, **10**, 495.

37 M. H. Lee, N. Lim, D. J. Ruebusch, A. Jamshidi, R. Kapadia, R. Lee, T. J. Seok, K. Takei, K. Y. Cho and Z. Fan, *Nano letters,* 2011, **11**, 3425-3430.

38 Y. Gogotsi and P. Simon, *Science Magazine,* 2011, **334**, 917-918.

39 D. P. Dubal, D. Aradilla, G. Bidan, P. Gentile, T. J. Schubert, J. Wimberg, S. Sadki and P. Gomez-Romero, *Scientific reports,* 2015, **5**, 9771.

40 S. Santhanagopalan, A. Balram and D. D. Meng, *ACS nano,* 2013, **7**, 2114-2125.

41 X. Lu, M. Yu, T. Zhai, G. Wang, S. Xie, T. Liu, C. Liang, Y. Tong and Y. Li, *Nano letters,* 2013, **13**, 2628-2633.

42 J. Xu, Q. Wang, X. Wang, Q. Xiang, B. Liang, D. Chen and G. Shen, *ACS nano,* 2013, **7**, 5453-5462.